Curvature-Induced Cell Rearrangements in Biological Tissues

Yuting Lou,[1,*] Jean-Francois Rupprecht,[1,2,†] Sophie Theis,[3] Tetsuya Hiraiwa,[1,‡] and Timothy E. Saunders[1,3,§]
[1]*Mechanobiology Institute, National University of Singapore, Singapore 117411, Singapore*
[2]*Aix Marseille Univ, Université de Toulon, CNRS, CPT (UMR 7332), Turing Centre for Living systems, Marseille, France*
[3]*Division of Biomedical Sciences, Warwick Medical School, University of Warwick, Coventry, CV4 7AL, United Kingdom*

(Received 19 May 2022; accepted 13 January 2023; published 6 March 2023)

On a curved surface, epithelial cells can adapt to geometric constraints by tilting and by exchanging their neighbors from apical to basal sides, known as an apico-basal topological transition 1 (AB-T1). The relationship between cell tilt, AB-T1s, and tissue curvature still lacks a unified understanding. Here, we propose a general framework for cell packing in curved environments and explain the formation of AB-T1s from the perspective of strain anisotropy. We find that steep curvature gradients can lead to cell tilting and induce AB-T1s. Alternatively, pressure differences across the epithelial tissue can drive AB-T1s in regions of large curvature anisotropy. The two mechanisms compete to determine the impact of tissue geometry and mechanics on optimized cell rearrangements in three dimensions.

DOI: 10.1103/PhysRevLett.130.108401

As the external surfaces and barriers of many organs, epithelial tissues have to mechanically adapt to their environment [1,2]. Extensive research into cell shape in two [3–10] and three dimensions [11–14] has revealed insights into how cells pack and undergo rearrangement during epithelial tissue formation [7–10,15]. Cellular dynamic processes, like division and apoptosis, can rearrange cell neighbors. T1 transitions—the exchange of neighbors without altering the cell number—is another ubiquitous mechanism of cell rearrangements [16,17]. T1 transitions are important in mediating planar tissue dynamics. For example, oriented T1 transitions can lead to tissue elongation or flow [15,18–20], and the energetic barriers for T1 transitions to occur can dictate tissue fluidity or solidity [9,21–23].

For a cell monolayer under 3D geometric constraint, cells can undergo apico-to-basal topological transitions (AB-T1s) [Fig. 1(a)]. Different from the planar T1 transitions, which are dynamic, AB-T1s are a static exchange of neighbors from the apical to basal membranes of the cells, leading to a specific 3D cell geometry, termed "scutoid" [24]. These arrangements have been observed in foams [25,26] and biological systems with curved surfaces [27–33].

Tissue curvature is proposed to be pivotal in inducing AB-T1s. In the ellipsoidal early *Drosophila* embryo, AB-T1s appear most frequently around 20–50 μm from the embryo head, a region with low curvature anisotropy but large tilt of cell lateral membranes [29] [Fig. 1(b)]. During salivary gland formation in the *Drosophila* embryo, AB-T1s occur at maximal curvature anisotropy [24]. Models have been proposed for cell packing in these specific cases [24,29], but there is currently no consensus on how curvature induces AB-T1s.

Here, we provide a framework for describing curvature-induced cell deformation, which can be generalized to an array of geometries, and discuss the interplay between cell mechanics and tissue geometry in inducing AB-T1s. We demonstrate that in 3D environments with steep curvature gradient, cells can tilt in order to pack efficiently. These tilted lateral membranes can exert tensions that contribute to in-plane stresses of opposite signs on the apical and

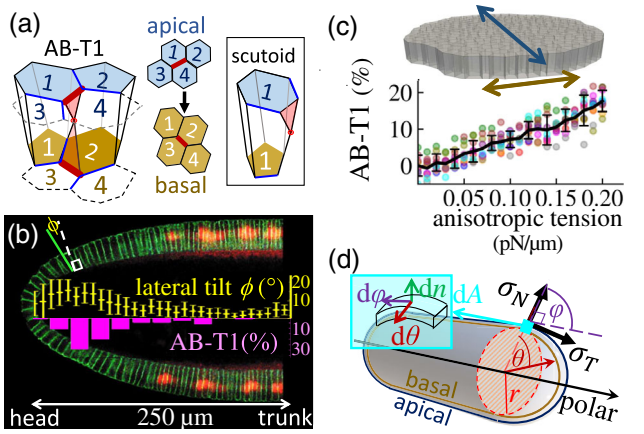

FIG. 1. Apical-basal topological transition 1 (AB-T1) in epithelial tissues. (a) Exchange of neighbor pair from 1-4 (apical) to 2-3 (basal), leading to an irregular 3D cell shape. (b) Tilt angle of lateral membrane (yellow) and percentage of cells undergoing at least one AB-T1 peaks near the head of a wild type *Drosophila* embryo, adapted from Ref. [29] under the license CC BY-NC-SA 3.0. (c) 3D vertex model simulation (10 sessions represented by colored dots). The session-averaged percentage of cells undergoing at least one AB-T1 (black curve) grows linearly with the magnitude of external tensions applied to the apical and basal membranes in orthogonal directions (two arrows on the top panel). (d) A two-shell model for curved epithelia on an axisymmetric object and the coordinates for an infinitesimal surface dA (cyan). The surface is subjected to tangential (σ_T) and normal (σ_N) external loads.

basal sides, thereby leading to AB-T1s. Conversely, when hydrostatic pressure dominates, we find that AB-T1s occur largely in regions with high curvature anisotropy. Overall, we show that the combination of tissue curvature, pressure, and lateral tensions determines the location of AB-T1 events.

Framework.—We treat the epithelia as a material composed of two connected thin shells, representing the apical and basal membrane surfaces. We assume the radius of curvature is significantly larger than the cell size so that, locally, cell membranes can be considered as flat at the apical and basal surfaces. Since the cell membrane thickness is even smaller than the cell diameter, we can use a continuum mechanics model based on membrane theory for elastic thin shells, neglecting bending stresses. Lateral membranes are included as part of the external load on the shell.

In a 2D shell model, the change of stresses over the membrane thickness are deemed as irrelevant at the scale of the whole system, and thus we can integrate them over the thickness, which yields tensions in-plane with unit N/m. The in-plane tensions in the apical or basal surface are described as a tensor $\hat{\tau}$ bearing two principal tensions $\tau_{\delta\delta}$, $\tau_{\nu\nu}$, and a shear stress component $\tau_{\delta\nu}$, with δ, ν being orthogonal coordinates in-plane. Negative signs indicate compressions. This tensor $\hat{\tau}$ can be decomposed into an isotropic part $\hat{\tau}_{\mathrm{iso}} = \frac{1}{2}\mathrm{Tr}(\hat{\tau})I$, corresponding to isotropic forces that induce local expansion or shrinkage of cell areas, and an anisotropic part $\hat{\tau}_{\mathrm{ani}} = \hat{\tau} - \hat{\tau}_{\mathrm{iso}}$ corresponding to those inducing shearing or anisotropic bulk compression or stretching.

AB-T1 transitions.—Stresses within the apical or basal membranes can induce cell shape changes and cell intercalations. Here, we assume that prior to any applied external load, cells are relaxed to isotropic shapes. The tendency for AB-T1s to occur will increase when the apical and basal sides are subjected to anisotropic stress [34]. To test this idea in three dimensions, we numerically simulated (using Tyssue [35], further details in the Supplemental Material, Sec. A [36]) the relaxation dynamics of a 3D tissue monolayer in a flat plane after applying anisotropic external tensions in-plane [Fig. 1(c) and movie S1 [36]]. The tensions applied to the apical and basal membranes are orthogonally orientated with respect to each other, with the same magnitude. The percentage of cells undergoing AB-T1s scaled linearly with the tension magnitude. At a steady state, the two external tensions are balanced by the in-plane stresses, which induces apico-basal difference in the anisotropic strain.

We next define a dimensionless measure for the AB-T1 tendency, γ. The magnitude of γ needs to be proportional to the percentage of cells undergoing AB-T1s, with the sign denoting the direction of AB-T1s (Supplemental Material, Eq. A.5 [36]). From vertex model simulations, this measure γ is approximately proportional to the apico-basal difference in the anisotropic strain (Fig. S1 [36]). In the absence of shear component $\tau_{\delta\nu}$, this proportionality reads

$$\gamma \propto \frac{\tau^a_{\delta\delta} - \tau^a_{\nu\nu}}{\mu^a} - \frac{\tau^b_{\delta\delta} - \tau^b_{\nu\nu}}{\mu^b}. \tag{1}$$

Without loss of generality, we set the proportionality coefficient in Eq. (1) to be 1. The denominators $\mu^{a,b}$ represent the effective stiffness (with unit N/m) of cell membranes. $\gamma > 0$ corresponds to cells that are stretched along the δ axis at the apical side while compressed along the ν axis at the basal side.

For the membrane stiffness μ, we recall the well-studied liquid foam model [42,43] whereby the elastic modulus of a foam (with unit Pa) scales to film surface tension over the bubble size. In our cell system, for simplicity we take $\mu^{a,b} = |\mathrm{Tr}(\hat{\tau}^{a,b})|$, assuming the isotropic tension contributes most to the surface tension. Alternative hypotheses for $\mu^{a,b}$—e.g., constant $\mu^{a,b}$—lead to similar results [44].

Force balance in axisymmetric shells.—Motivated by the *Drosophila* embryo, salivary gland and oocyte geometries, we focus on axisymmetric geometries, which have rotational symmetry about a polar axis [Fig. 1(d)]. For any infinitesimal surface element dA on the 3D curved shell, it has a normal direction $\overrightarrow{dn}$, and two tangential directions along the meridian $\overrightarrow{d\varphi}$ and latitudinal radii $\overrightarrow{d\theta}$. We hereafter replace δ and ν by φ and θ.

The tensions are balanced by the external loads exerted on the shell surface. These external loads can have origins from passive cell geometry control or cellular active forces [45,46]. Here, we only consider axisymmetric external load, which can be decomposed into a normal part σ_N (positive pointing outward) and a tangential part along the meridian σ_T (positive pointing to the head) and hence the in-plane shear $\tau_{\theta\varphi} \approx 0$. The meridional tension $\tau_{\varphi\varphi}$ integrated over the perimeter of any local cut [red ring in Fig. 1(d)] is balanced in the polar direction by the accumulated force over the revolved surface as

$$\tau_{\varphi\varphi} 2\pi r \sin\varphi = \int_0^{s(\varphi)} [\sigma_N \cos\varphi + \sigma_T \sin\varphi] 2\pi r ds, \tag{2}$$

where r is the distance to the polar axis from the local surface dA and ds is the meridional arc length [Fig. 1(d)], with $\cos\varphi$ and $\sin\varphi$ projecting tensions onto the polar axes (Supplemental Material, Sec. B [36]).

The circumferential tension $\tau_{\theta\theta}$ is derived from force balance along the normal direction of the surface:

$$C_{\varphi\varphi}\tau_{\varphi\varphi} + C_{\theta\theta}\tau_{\theta\theta} = \sigma_N, \tag{3}$$

where the principal curvatures are denoted as $C_{\varphi\varphi}$ along the meridional direction and $C_{\theta\theta} = \sin\varphi/r$.

In the case when external loads are hydrostatic ($\sigma_T = 0$ and $\sigma_N = P$), large strain anisotropy appears with large curvature anisotropy $|C_{\varphi\varphi}/C_{\theta\theta} - 1|$. If the two surfaces are subject to the normal loading with the same sign $\sigma_N^a/\sigma_N^b > 0$, the magnitude of γ is negligible; otherwise, with $\sigma_N^a/\sigma_N^b < 0$, γ has its maximal value always at the region of high curvature anisotropy, e.g., in the trunk region of the embryo (Supplemental Material, Sec. C [36]).

Cell tilting.—The above hydrostatic explanation is not consistent with findings in the early *Drosophila* embryo, where the AB-T1s occurred near, but not exactly at, the tip, which has isotropic surface curvatures. Here, we show the explanation could lie in the tilt of cells towards the head, as visible in Fig. 1(b). Tilt of lateral membranes affects the external load profiles σ_T, σ_N and hence we conjecture that tilting plays a role in inducing AB-T1s.

To better understand the interplay between curvature and cell tilt, we consider an arbitrary axisymmetric geometry with half meridian length s_0 and a distance between apical and basal sides $e(s)$ [Figs. 2(a) and S2 in [36]]. The tilted lateral membrane leans by a small angle $\phi(s)$ away from the normal direction, resulting in a small meridional distance Δs between s and s' (the apical end of the tiled lateral membrane). Assuming $\Delta s(s) \ll e(s)$, the tilt angle is approximated as $\tan\phi(s) \sim \Delta s(s)/e(s)$. Considering the local cell density, Δs can be approximated by the cell number difference between the apical and basal surfaces [Fig. 2(a), sky blue and orange curves]:

$$\Delta s(s) \times 2\pi r^a(s) \times \rho^a(s) \sim N^a(s) - N^b(s), \qquad (4)$$

where $N^{(a,b)}(s) = \int_0^s \rho^{a,b} dA^{a,b}(s)$ are the accumulated cell number from the head apex to the coordinate s, $\rho^{a,b}(s)$ are the densities at the apical or basal surfaces, and $r^a(s)$ is the distance from s at the apical side to the polar axis. Subsequently, the tilt ϕ reads

$$\tan\phi(s) \sim \frac{N^b(s)(N^b(s_0) - N^b(s))[\overline{q(s_1)} - \overline{q(s_2)}]}{2\pi e(s) r^a(s) N^b(s_0)}, \qquad (5)$$

where $q(s) = e(s)[C_{\varphi\varphi}(s) + C_{\theta\theta}(s)] + e^2(s) C_{\varphi\varphi}(s) C_{\theta\theta}(s)$ is the effective tissue mean curvature relative to the cell height. The $\overline{q(s_1)}$ and $\overline{q(s_2)}$ are $q(s)$ weighted by cell numbers in a range of $0 < s_1 < s$ and $s < s_2 < s_0$, respectively. For a convex object, a large magnitude of ϕ at s corresponds to a large gradient of $q(s)$ and the tilt leans towards the region of higher convex curvature (e.g., the head of embryo).

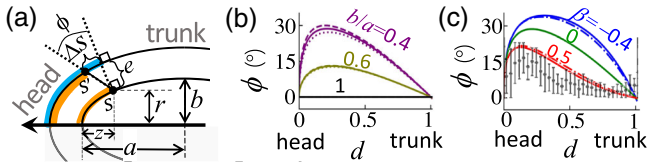

FIG. 2. Cell tilting under cell-volume conservation. (a) A meridional cross section view of a two-shelled prolate ellipsoid in the 1/4 quadrant. The orange curves are the apical and basal surfaces shared by the same cells; the sky blue curve is the apical normal projection of the basal orange curve. (b) The lateral tilt angle profile [Eq. (5)] vs the polar direction $d = z/a$ on a prolate ellipsoid under varying inverse aspect ratio b/a. Solid curves represent cell height with $e = 0.1a$, dashed $e = 0.01a$, and dotted $e = 0.3a$. (c) Tilt profiles under varying cell height gradient β, with $b/a \sim 0.4$, $e/a \sim 0.1$. Dash-dotted curves correspond to a homogeneous density being imposed. Gray dots correspond to experimental data observed in the early *Drosophila* embryo ($\beta \sim 0.5$) with s.d., adapted from Ref. [29].

Tilt in ellipsoidal geometries.—We now apply this formalism to a prolate ellipsoidal geometry as shown in Fig. 2(a), with major half axis a and minor half axis b (parametrization in Supplemental Material, Sec. D [36]). We use cell height profiles, $e(s)$, based on tissue height changes observed experimentally [29]. For simplicity, we consider the leading order in the arc length s from the head, giving the height profile as $e(s) \approx \varepsilon[1 + \beta(s/s_{1/4} - 0.5)]$ for $s \in [0, s_{1/4}]$, where $s_{1/4}$ is the 1/4 perimeter of the meridian ellipse and ε is the average cell height across the surface and β is the gradient of cell height change across the surface, with $\beta = 0$ representing homogeneous cell height.

We consider the cell tilt as a function of the relative distance to the head along a prolate ellipsoid $d(s)$; $d = 0$ corresponds to the head and $d = 1$ to the trunk. The elongation of the ellipsoid (smaller b/a) promotes tilting [Fig. 2(b)] significantly, whereas the magnitude of cell height ε has a negligible impact on the tilt profile [see different line types in Fig. 2(b)]. For a typical geometry observed experimentally in *Drosophila* ($b/a \sim 0.4$, $e/a \sim 0.1$ [29]), the tilt angle peaks around 30° [Fig. 2(c)]. The cell height gradient β generates a reduced tilt angle but the peak angle is more pronounced. Given the experimentally measured value ($\beta \sim 0.5$), the numerical tilt profile (red) is similar to experimental measurements [gray dots in Fig. 2(c), adapted from [29]].

We have taken cell density to either satisfy a constant cell volume condition $e(s)/\rho(s) = \text{const.}$ [straight curves in Fig. 2(c)] or have homogeneous cell density $\rho(s) = \text{const.}$ [dash-dotted curves in Fig. 2(c)]. The difference between the two conditions is negligible, indicating that cell density is insignificant compared to geometry in determining tilt angle. This enables us to remove $\rho(s)$ from further calculations.

Tensions in ellipsoidal geometries.—Next, we consider the following external loads on the cell surfaces: pressure from the outside P_{out}; from the internal cavity (e.g., yolk or luminal pressure) P_{in}; internal cell pressure P_T; and the lateral stress dipoles T along the lateral membranes in the system [Fig. 3(a)]. The pressure differences at the apical and basal surfaces are given by $\Delta\Pi^a = P_T - P_{\text{out}}$ and $\Delta\Pi^b = P_{\text{in}} - P_T$, respectively, with positive $\Delta\Pi$ pointing

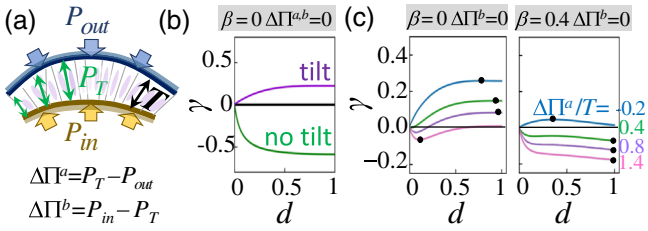

FIG. 3. AB-T1 tendency γ calculated for a prolate ellipsoid with $b/a = 0.4$. (a) Schematic illustration of the system under pressure and the stress dipole T along the lateral sides. (b) Comparison of γ profiles between the cases with and without cell tilt (indicated by purple and green curves, respectively), with a constant tissue height $e = 0.05a$. The black line ($\gamma = 0$) indicates the result for the sphere case as a reference. (c) γ profiles under varying pressure differences $\Delta\Pi^a$ with $\Delta\Pi^b = 0$. Black dots indicate where $|\gamma|$ reaches its maximum.

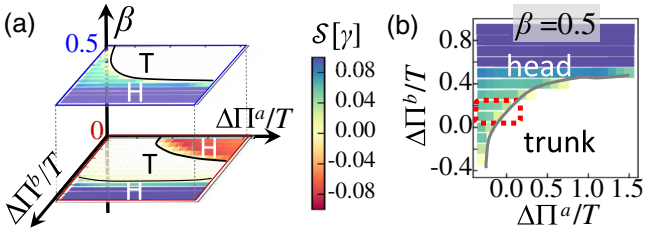

FIG. 4. Phase diagrams for the location of peaked AB-T1 transition tendency. (a)–(b) Color indicates prominence of peak $\mathcal{S}[\gamma] = \mathrm{sign}(\gamma_{\mathrm{peak}}) \times ||\gamma_{\mathrm{peak}}| - |\gamma_{\mathrm{trunk}}||$, where "peak" refers to maximal $|\gamma|$. The phase boundaries detected by contours ($d_{\mathrm{peak}} = 0.5$) separate the trunk (T) and the head (H) regions. The region enclosed by red dashed box in (b) corresponds to the experimental setting near the *Drosophila* head. See Fig. S4 [36] for more details.

towards the outside. The external normal and tangential loads on the apical and basal side are $\sigma_N^a = \Delta\Pi^a + T\cos\phi$, $\sigma_T^a = \Delta\Pi^a + T\sin\phi$, $\sigma_N^b = \Delta\Pi^b + T\cos\phi$, and $\sigma_T^b = \Delta\Pi^b - T\sin\phi$. Epithelial tissues can be found under tension or compression [47,48], hence we allow the pressure and tensions to be either positive or negative to keep a generic picture.

In a pressure-free setting $\Delta\Pi^{a,b} = 0$ with homogeneous tissue height $\beta = 0$, cell tilt induces qualitative differences in the tension across the cell surfaces, resulting in AB-T1s [Fig. 3(b)]. The stress dipole T along the tilted lateral membranes exerts tangential stresses with opposite directions in the apical and basal planes. Consequently, γ [Eq. (1)] flips its sign depending on there being cell tilt [Fig. 3(b), purple] or not [Fig. 3(b), green]. However, this qualitative difference vanishes when the surface approaches a sphere ($a/b = 1$) [Fig. 3(b), black line]. The profiles of the resultant tensions $\tau_{\theta\theta}$ and $\tau_{\varphi\varphi}$ are presented in Fig. S3 [36].

When the pressure difference is comparable with lateral stress ($\Delta\Pi^{a,b} \sim T$), the profile of γ is sensitive to the pressure difference $\Delta\Pi^{a,b}$ and the tissue geometry β [Fig. 3(c)]. As the pressure difference varies, the peak of $|\gamma|$ [black dots in Fig. 3(c)] can shift from the trunk ($d = 1$) to the head ($d \ll 1$) for $\beta = 0$, and in the opposite manner for $\beta = 0.4$. This indicates that the location of maximal tendency for AB-T1s can be sensitive to geometry and cellular forces.

We next constructed phase diagrams, using the two pressure differences relative to lateral tension $\Delta\Pi^{a,b}/T$ and the tissue height gradient β as control parameters. For the order parameter, we define a mapping $\mathcal{S}$ from the γ profiles as $\mathcal{S}[\gamma] = \mathrm{sign}(\gamma_{\mathrm{peak}}) \times ||\gamma_{\mathrm{peak}}| - |\gamma_{\mathrm{trunk}}||$, where $\gamma_{\mathrm{peak}} \equiv \gamma(d_{\mathrm{peak}})$ with $d_{\mathrm{peak}} = \mathrm{argmax}_d|\gamma(d)|$ represents the peak value of $|\gamma|$. The sign of $\mathcal{S}[\gamma]$ indicates the orientation of AB-T1s found at the largest AB-T1 tendency, with the magnitude describing how the tendency is enhanced compared to that at the trunk. $S = 0$ denotes no significant AB-T1s occurring away from the trunk.

The phase diagrams in Figs. 4(a)–4(b) provide a panoramic view of the interplay between the mechanics and geometry on the number, location, and orientation of AB-T1s within a curved tissue. In the space of $\Delta\Pi^a - \Delta\Pi^b - \beta$ the peaked tendency for AB-T1s switches from trunk to head within different control parameter regimes. In range of $\Delta\Pi^b/T \ll 1$, tissue height gradient β modulates the emergence of AB-T1s with different orientations. See also Fig. S4 [36] for further details of the diagrams.

In the specific case of the *Drosophila* early embryo, the pressure difference across the basal side appears to be weak as compared with the growing stresses from the lateral membranes, which suggests that $\Delta\Pi^b/T \sim 0$. Given the measured tissue height gradient ($\beta \approx 0.5$), the range enclosed by the dashed rectangle in Fig. 4(b) suggests that the embryo bears overall negligible pressure for having AB-T1s near the head. Cell tilting can play an important role, by enhancing the strain anisotropy difference between the apical and basal surfaces.

Conclusions.—We have proposed a two-elastic-shell model to describe the mechanics in curved biological tissues. We first show that the occurrence of AB-T1s scales with the strain anisotropy difference between apical and basal sides. Then we find that the interplay between mechanics (e.g., pressure, lateral tension) together with the cellular tilt determine the location with most number of neighbor rearrangements along the apico-basal direction. Our formalism provides predictions for the location of AB-T1s that are echoed by experimental observations in various geometries [24,29].

The lateral membranes play an essential role in balancing stress across the cell, thereby regulating cell shape. In particular, tilting of cell lateral membranes, in conjunction with pressure and tissue thickness, results in a rich phase diagram for the locations of AB-T1s. Without the lateral tilting, AB-T1s are driven by hydrostatic stresses at regions with large curvature anisotropy, as observed in tubular structures [24]. On the contrary, stresses along tilted lateral

membranes could induce AB-T1s mostly at the regions with large gradient of curvatures, as observed in early *Drosophila* embryo [29].

Though we have focused on a prolate geometry with simple external loads, our formalism can be generalized to a diverse range of tissue geometries observed *in vivo*. We expect tilt to occur at the steepest curvature gradient, even for nonaxisymmetric and nonclosed surface geometries; e.g., the brain and gut [49]. We can also explore the role of in-plane shear and bending within this theoretical framework. Internal cell strain, which is likely significant during cellular processes such as cell division [50], can also be considered as a source of external loading to the shell of apical and basal membranes. Finally, transient and reversible AB-T1s have been observed [51,52]; the dynamic aspect of AB-T1s may be relevant to the mechanism of T1 transitions [23,34] and their contributions to processes like tissue folding or buckling [53–58] remains to be investigated.

We thank Jacques Prost for discussion leading to Eq. (4). T. H. and T. E. S. are funded by Mechanobiology Institute seed grants. T. E. S. and S. T. are funded by an EPSRC Physics of Life grant (R.MRCB.1137) and startup support from the University of Warwick. J.-F. R. has received funding from France 2030, the French Government program managed by the French National Research Agency (ANR-16-CONV-0001) and from the Excellence Initiative of Aix-Marseille University—A*MIDEX.

*mbilouy@nus.edu.sg
†jean-francois.rupprecht@univ-amu.fr
‡mbithi@nus.edu.sg
§Lead contact: timothy.saunders@warwick.ac.uk

[1] C. Guillot and T. Lecuit, Mechanics of epithelial tissue homeostasis and morphogenesis, Science **340**, 1185 (2013).
[2] E. Latorre, S. Kale, L. Casares, M. Gómez-González, M. Uroz, L. Valon, R. V. Nair, E. Garreta, N. Montserrat, A. Del Campo *et al.*, Active superelasticity in three-dimensional epithelia of controlled shape, Nature (London) **563**, 203 (2018).
[3] B. Aigouy, R. Farhadifar, D. B. Staple, A. Sagner, J.-C. Roper, F. Julicher, and S. Eaton, Cell flow reorients the axis of planar polarity in the wing epithelium of *drosophila*, Cell **142**, 773 (2010).
[4] A. Sagner, M. Merkel, B. Aigouy, J. Gaebel, M. Brankatschk, F. Jülicher, and S. Eaton, Establishment of global patterns of planar polarity during growth of the *drosophila* wing epithelium, Curr. Biol. **22**, 1296 (2012).
[5] N. Khalilgharibi, J. Fouchard, N. Asadipour, R. Barrientos, M. Duda, A. Bonfanti, A. Yonis, A. Harris, P. Mosaffa, Y. Fujita *et al.*, Stress relaxation in epithelial monolayers is controlled by the actomyosin cortex, Nat. Phys. **15**, 839 (2019).
[6] R. J. Tetley, M. F. Staddon, D. Heller, A. Hoppe, S. Banerjee, and Y. Mao, Tissue fluidity promotes epithelial wound healing, Nat. Phys. **15**, 1195 (2019).
[7] M. C. Gibson, A. B. Patel, R. Nagpal, and N. Perrimon, The emergence of geometric order in proliferating metazoan epithelia, Nature (London) **442**, 1038 (2006).
[8] R. Farhadifar, J.-C. Röper, B. Aigouy, S. Eaton, and F. Jülicher, The influence of cell mechanics, cell-cell interactions, and proliferation on epithelial packing, Curr. Biol. **17**, 2095 (2007).
[9] D. B. Staple, R. Farhadifar, J.-C. Röper, B. Aigouy, S. Eaton, and F. Jülicher, Mechanics and remodelling of cell packings in epithelia, Eur. Phys. J. E **33**, 117 (2010).
[10] L. Atia, D. Bi, Y. Sharma, J. A. Mitchel, B. Gweon, S. A Koehler, S. J. DeCamp, B. Lan, J. H. Kim, R. Hirsch *et al.*, Geometric constraints during epithelial jamming, Nat. Phys. **14**, 613 (2018).
[11] X. Du, M. Osterfield, and S. Y. Shvartsman, Computational analysis of three-dimensional epithelial morphogenesis using vertex models, Phys. Biol. **11**, 066007 (2014).
[12] M. Krajnc and P. Ziherl, Theory of epithelial elasticity, Phys. Rev. E **92**, 052713 (2015).
[13] A. G. Fletcher, F. Cooper, and R. E. Baker, Mechanocellular models of epithelial morphogenesis, Phil. Trans. R. Soc. B **372**, 20150519 (2017).
[14] M. Merkel and M. L. Manning, A geometrically controlled rigidity transition in a model for confluent 3d tissues, New J. Phys. **20**, 022002 (2018).
[15] C. Bertet, L. Sulak, and T. Lecuit, Myosin-dependent junction remodelling controls planar cell intercalation and axis elongation, Nature (London) **429**, 667 (2004).
[16] H. Honda, Y. Ogita, S. Higuchi, and K. Kani, Cell movements in a living mammalian tissue: Long-term observation of individual cells in wounded corneal endothelia of cats, J. Morphol. **174**, 25 (1982).
[17] A. G. Fletcher, M. Osterfield, R. E. Baker, and S. Y. Shvartsman, Vertex models of epithelial morphogenesis, Biophys. J. **106**, 2291 (2014).
[18] H. Honda, T. Nagai, and M. Tanemura, Two different mechanisms of planar cell intercalation leading to tissue elongation, Dev. Dyn. **237**, 1826 (2008).
[19] K. Sato, T. Hiraiwa, E. Maekawa, A. Isomura, T. Shibata, and E. Kuranaga, Left–right asymmetric cell intercalation drives directional collective cell movement in epithelial morphogenesis, Nat. Commun. **6**, 10074 (2015).
[20] T. Hiraiwa, E. Kuranaga, and T. Shibata, Wave propagation of junctional remodeling in collective cell movement of epithelial tissue: Numerical simulation study, Front. Cell Dev. Biol. **5**, 66 (2017).
[21] D. Bi, J. Lopez, J. M. Schwarz, and M. L. Manning, A density-independent rigidity transition in biological tissues, Nat. Phys. **11**, 1074 (2015).
[22] D. Bi, X. Yang, M. C. Marchetti, and M. L. Manning, Motility-Driven Glass and Jamming Transitions in Biological Tissues, Phys. Rev. X **6**, 021011 (2016).
[23] M. Krajnc, S. Dasgupta, P. Ziherl, and J. Prost, Fluidization of epithelial sheets by active cell rearrangements, Phys. Rev. E **98**, 022409 (2018).
[24] P. Gómez-Gálvez, P. Vicente-Munuera, A. Tagua, C. Forja, A. M. Castro, M. Letrán, A. Valencia-Expósito, C. Grima, M. Bermúdez-Gallardo, Ó. Serrano-Pérez-Higueras *et al.*, Scutoids are a geometrical solution to three-dimensional packing of epithelia, Nat. Commun. **9**, 1 (2018).

[25] E. B. Matzke, The three-dimensional shape of epidermal cells of the apical meristem of anacharis densa (elodea), Am. J. Bot. **35**, 323 (1948).
[26] A. Mughal, S. Cox, D. Weaire, S. Burke, and S. Hutzler, Demonstration and interpretation of 'scutoid' cells formed in a quasi-2d soap froth, Philos. Mag. Lett. **98**, 358 (2018).
[27] G. Blanchard, A 3d cell shape that enables tube formation, Nature (London) **561**, 182 (2018).
[28] P. Gómez-Gálvez, P. Vicente-Munuera, S. Anbari, J. Buceta, and L. M. Escudero, The complex three-dimensional organization of epithelial tissues, Development **148**, dev195669 (2021).
[29] J.-F. Rupprecht, K. H. Ong, J. Yin, A. Huang, H.-H.-Q. Dinh, A. P. Singh, S. Zhang, W. Yu, and T. E. Saunders, Geometric constraints alter cell arrangements within curved epithelial tissues, Mol. Biol. Cell **28**, 3582 (2017).
[30] Y. E. Sanchez-Corrales, G. B. Blanchard, and K. Röper, Radially patterned cell behaviours during tube budding from an epithelium, eLife **7**, e35717 (2018).
[31] C. M. Nelson, Epithelial packing: Even the best of friends must part, Curr. Biol. **28**, R1197 (2018).
[32] K. Z. Perez-Vale and M. Peifer, Orchestrating morphogenesis: Building the body plan by cell shape changes and movements, Development **147**, dev191049 (2020).
[33] C. Pérez-González *et al.*, Mechanical compartmentalization of the intestinal organoid enables crypt folding and collective cell migration, Nat. Cell Biol. **23**, 745 (2021).
[34] C. Duclut, J. Paijmans, M. M. Inamdar, C. D. Modes, and F. Jülicher, Nonlinear rheology of cellular networks, Cells Dev. **168**, 203746 (2021).
[35] S. Theis, M. Suzanne, and G. Gay, Tyssue: An epithelium simulation library, J. Open Source Softwaare **6**, 2973 (2021).
[36] See Supplemental Material at http://link.aps.org/supplemental/10.1103/PhysRevLett.130.108401 for the detailed explanations on the models and the derivations of the equations, which includes Refs. [37–41].
[37] S. Okuda, Y. Inoue, M. Eiraku, Y. Sasai, and T. Adachi, Reversible network reconnection model for simulating large deformation in dynamic tissue morphogenesis, Biomech. Model. Mechanobiol. **12**, 627 (2012).
[38] F. Graner, B. Dollet, C. Raufaste, and P. Marmottant, Discrete rearranging disordered patterns, part i: Robust statistical tools in two or three dimensions, Eur. Phys. J. E **25**, 349 (2008).
[39] P. M. Naghdi, The theory of shells and plates, in *Linear Theories of Elasticity and Thermoelasticity* (Springer, New York, 1973), pp. 425–640.
[40] J. R. Barber, *Intermediate Mechanics of Materials* (Springer, New York, 2011).
[41] W. Flügge, *Stresses in Shells* (Springer Science & Business Media, New York, 2013).
[42] D. L. Weaire and S. Hutzler, *The Physics of Foams* (Oxford University Press, New York, 2001).
[43] I. Cantat, S. Cohen-Addad, F. Elias, F. Graner, R. Höhler, O. Pitois, F. Rouyer, and A. Saint-Jalmes, *Foams: Structure and Dynamics* (Oxford University Press, Oxford, 2013).
[44] Y. Lou, J.-F. Rupprecht, S. Theis, T. E. Saunders, and T. Hiraiwa, The interplay between geometry and cell mechanics determines 3d cell shape in curved environments (to be published) [Phys. Rev. E.].
[45] C. G. Vasquez and A. C. Martin, Force transmission in epithelial tissues, Dev. Dyn. **245**, 361 (2016).
[46] F.-L. Wen, Y.-C. Wang, and T. Shibata, Epithelial folding driven by apical or basal-lateral modulation: Geometric features, mechanical inference, and boundary effects, Biophys. J. **112**, 2683 (2017).
[47] S. Tlili, J. Yin, J.-F. Rupprecht, M. Mendieta-Serrano, G. Weissbart, N. Verma, X. Teng, Y. Toyama, J. Prost, and T. Saunders, Shaping the zebrafish myotome by intertissue friction and active stress, Proc. Natl. Acad. Sci. U.S.A. **116**, 25430 (2019).
[48] S. Sonam, L. Balasubramaniam, S.-Z. Lin, Y. M. Y. Ivan, I. P. Jaumà, C. Jebane, M. Karnat, Y. Toyama, P. Marcq, J. Prost *et al.*, Mechanical stress driven by rigidity sensing governs epithelial stability, Nat. Phys. **19**, 132 (2023).
[49] C. Pérez-González, G. Ceada, M. Matejčić, and X. Trepat, Digesting the mechanobiology of the intestinal epithelium, Curr. Opin. Genet. Dev. **72**, 82 (2022).
[50] H. F. Gomez, M. S. Dumond, L. Hodel, R. Vetter, and D. Iber, 3d cell neighbour dynamics in growing pseudostratified epithelia, eLife **10**, e68135 (2021).
[51] A. C. Martin and B. Goldstein, Apical constriction: Themes and variations on a cellular mechanism driving morphogenesis, Development **141**, 1987 (2014).
[52] Z. Sun, C. Amourda, M. Shagirov, Y. Hara, T. E. Saunders, and Y. Toyama, Basolateral protrusion and apical contraction cooperatively drive *drosophila* germ-band extension, Nat. Cell Biol. **19**, 375 (2017).
[53] E. Hannezo, J. Prost, and J.-F. Joanny, Instabilities of Monolayered Epithelia: Shape and Structure of Villi and Crypts, Phys. Rev. Lett. **107**, 078104 (2011).
[54] E. Hannezo, J. Prost, and J.-F. Joanny, Theory of epithelial sheet morphology in three dimensions, Proc. Natl. Acad. Sci. U.S.A. **111**, 27 (2014).
[55] S. Alt, P. Ganguly, and G. Salbreux, Vertex models: From cell mechanics to tissue morphogenesis, Phil. Trans. R. Soc. B **372**, 20150520 (2017).
[56] N. Harmand, A. Huang, and S. Hénon, 3d Shape of Epithelial Cells on Curved Substrates, Phys. Rev. X **11**, 031028 (2021).
[57] A. Trushko, I. Di Meglio, A. Merzouki, C. Blanch-Mercader, S. Abuhattum, J. Guck, K. Alessandri, P. Nassoy, K. Kruse, B. Chopard *et al.*, Buckling of an epithelium growing under spherical confinement, Dev. Cell **54**, 655 (2020).
[58] J. Fierling, A. John, B. Delorme, A. Torzynski, G. B. Blanchard, C. M. Lye, G. Malandain, BNat. Commun.. Sanson, J. Étienne, P. Marmottant *et al.*, Embryo-scale epithelial buckling forms a propagating furrow that initiates gastrulation, Nat. Commun. **13**, 3348 (2022).